Palladium deposition on copper(II) phthalocyanine/ metal organic framework composite and electrocatalytic activity of the modified electrode towards the hydrogen evolution reaction.

Renewable Energy 119 (2018) 62–72

Contents lists available at ScienceDirect

Renewable Energy

journal homepage: www.elsevier.com/locate/renene

Palladium deposition on copper(II) phthalocyanine/metal organic framework composite and electrocatalytic activity of the modified electrode towards the hydrogen evolution reaction

Gobeng R. Monama [a], Siyabonga B. Mdluli [b], Gloria Mashao [a], Mogwasha D. Makhafola [a], Kabelo E. Ramohlola [a], Kerileng M. Molapo [a], Mpitloane J. Hato [a, *], Katlego Makgopa [c], Emmanuel I. Iwuoha [b], Kwena D. Modibane [a, **]

[a] Department of Chemistry, School of Physical and Mineral Sciences, University of Limpopo (Turfloop), Polokwane, Sovenga 0727, South Africa
[b] SensorLab, Chemistry Department, University of the Western Cape, Bellville 7535, Cape Town, South Africa
[c] Department of Chemistry, Faculty of Science, Tshwane University of Technology (Acardia Campus), Pretoria 0001, South Africa

ARTICLE INFO

Article history:
Received 13 August 2017
Received in revised form
8 November 2017
Accepted 29 November 2017
Available online 30 November 2017

Keywords:
Metal-organic frameworks
Phthalocyanine
Palladium
Hydrogen evolution reaction
Hydrogen spillover

ABSTRACT

Pd-supported copper phthalocyanine/metal organic frameworks (Pd@CuPc/MOF) composite was synthesized by the reaction between CuPc and MOF followed by electroless Pd plating. The structural properties of MOF, Pd@MOF and Pd@CuPc/MOF composite were characterized using X-ray diffraction (XRD), Fourier transform infrared (FTIR), simultaneous thermal analysis (STA), ultraviolet–visible spectroscopy (UV–vis), scanning electron microscopy (SEM/EDS) and Brunauer-Emmett-Teller (BET). The XRD, UV–vis and FTIR analyses showed that Pd was coated on CuPc/MOF composite. SEM and EDS results revealed that Pd nanoparticles were well-dispersed and anchored tightly on the composite. The thermal stability of MOF increased upon addition of Pd and CuPc. The electrochemical hydrogen evolution reaction (HER) performance of the synthesized materials was studied by cyclic voltammetry (CV) and Tafel analysis. The Tafel slope of the composite was 176.9 mV/dec and the transfer coefficient of 0.67 which is close to 0.5. The HER results revealed that the Pd@CuPc/MOF composite has better catalytic characteristic such as high catalytic activity and lowest onset potential compared to MOF. More importantly, the significant enhancement of HER performance at ambient temperature for the composite with Pd content can be ascribed to the hydrogen spillover mechanism in such system.

1. Introduction

The growing concern of energy crisis and environmental pollution promotes the development of an effective clean energy technology. Hydrogen gas has a potential to be an alternative energy carrier because it offers clean, efficient and renewable energy characteristics [1]. In addition, H_2 gas yields more energy, which is about 2.75 times greater as compared to traditional gasoline based energy resources [2]. However, the problem for practical usage of H_2 gas as an energy carrier lies in the production and storage technology [2,3]. Electrochemical water splitting ($H_2O \rightarrow H_2 + ½ O_2$) consists of two half reactions known as oxygen reduction reaction (ORR) and hydrogen evolution reaction (HER) [3]. The ORR and HER normally take place on the anode and the cathode, respectively. The reaction mechanism of HER ($2H+ + e- \rightarrow H_2$) in aqueous acid or alkaline solutions proceeds in a series of three elementary reaction steps which comprise of two electrochemical reactions and one chemical reaction [4]. In acidic medium, the HER could proceed via three main steps given in Eqs. (1)–(3) [5]:

$H^+ + e- \rightarrow$ Had Volmer reaction (electrochemical adsorption) (1)

Had + $H^+ + e- \rightarrow$ H2 Heyrovsky reaction (electrochemical desorption) (2)

Had + Had $\rightarrow H_2$ Tafel reaction (catalytic desorption) (3)

* Corresponding author.
** Corresponding author.
E-mail addresses: mpitloane.hato@ul.ac.za (M.J. Hato), kwena.modibane@ul.ac.za (K.D. Modibane).

https://doi.org/10.1016/j.renene.2017.11.084
0960-1481/

The first step (Eq. (1)) is the Volmer reaction in which a proton receives an electron and generates an adsorbed hydrogen atom (Had) at the active site as an intermediate [6]. The second step can either be Heyrovsky or Tafel reaction. In Volmer-Heyrovsky mechanism, a proton from a water layer reacts with one adsorbed hydrogen to form H_2 as illustrated in Eq. (2). In the Volmer-Tafel mechanism, two adsorbed surface hydrogens next to each other react to form H_2 molecule as illustrated in Eq. (3) [7]. The two steps of hydrogen adsorption and desorption on the catalyst surface are competitive in nature. A catalyst surface having too weak bonding strength with hydrogen atoms cannot efficiently adsorb the reactant to initiate the HER and a catalyst surface having too strong bonding strength would have a difficulty in releasing the product towards completion of the HER [7,8]. Therefore, a suitable catalyst for HER should have a good balance between adsorption and desorption steps [9]. Up to date, platinum (Pt)-based electrocatalysts have been known as efficient catalysts for hydrogen production owing to their excellent catalytic performance [10]. However, their widespread application has been restricted by their high cost and low-earth abundance [11]. Therefore, it is necessary to synthesize material suitable for electrochemical studies as an alternative to Pt.

Non-precious metal catalysts such as transition-metal sulfides, phosphides and alloys have attracted main research interest as HER materials owing to their excellent electrical conductivity and good durability [11]. HER is a predominantly surface dictated phenomenon, which depends largely on the shape, size, interface, porosity and composition of the material in enhancing the H2 evolution and decreasing the overpotential [12]. In order to improve the catalytic performance, the electrocatalysts should possess a three-dimensional (3D) porous polyhedral structure, which could provide a large surface area, luxuriant electrocatalytic active sites and easier interconnected electron-transfer access [3]. A number of porous materials such as carbon nanotubes, metal organic frameworks (MOFs), graphite nanofibers, zeolites and activated carbon were proposed as candidates for HER [1,9,13]. Among these materials, MOFs hold a greater promise as potential candidates in the design of advanced multifunctional materials due to their unique structures [14]. MOFs are inorganic-organic hybrid compounds built from metal ions or clusters and organic ligands by coordination bonds, providing highly crystalline porous structures with large surface area, high pore volume as well as uniform nanoscale cavities [15]. Thus, MOFs have been used in various applications such as energy storage, CO_2 adsorption, hydrocarbon adsorption/separation, catalysis, advanced sorbents for solids extraction and sensors [16,17]. However, MOFs possess some drawbacks as HER material because of H_2 embrittlement, moisture instability and poor H_2 adsorption and desorption at ambient conditions [18]. There are few strategies including dopant modification, entrapping functional molecules or nanoparticles within the framework and post-synthesis method to optimize their structural properties in order to improve MOFs weaknesses for HER application [19]. Lin et al. [20] reported MOF-$CoSe_2$ delivers excellent HER performance with low Tafel slope (42 mV dec-1), small overpotential (150 mV), and remarkable stability, which can be attributed to the unique MOFs structure with $CoSe_2$ nanoparticles anchored into nitrogen-dope to the unique MOFs structure with $CoSe_2$ nanoparticles anchored into nitrogen-doped (N-doped) graphitic carbon. Furthermore, it has been demonstrated that the heat of adsorption can be improved by introducing open metals sites as a result of reducing the pore size [20,21]. Accordingly, the hydrogen spillover effect for enhanced uptakes of hydrogen at ambient temperature (298 K) on adsorbents has attracted much attention from the viewpoint of practical applications [22-24]. This spillover mechanism is well documented in catalysis and consists of the dissociation of three times higher storage values at room temperature have recently been reported for noble metal-doped MOFs [24]. In particular, palladium is well known as a hydrogen-spillover metal and an effective catalyst for reactions owing to its strong affinity to hydrogen [25]. However, the reproducibility of hydrogen spillover enhancement by Pd@MOF bridging method is affected by many factors, including contacts between the dissociation source and receptor, metal particle sizes and doping method [25]. Metallophthalocyanines (MPcs) incorporated into porous MOF materials can enhance and generate new functionalities on the building blocks. This is because the porphyrin containing building blocks can be stabilized in the formed solid frameworks, while the pore structures of the framework materials can lead to their differential recognitions of the substrates. Furthermore, the catalytic functionalities of the porous porphyrinic framework materials can be easily realized by modulating catalytic-active metal sites and tailoring the peripheral environments of metalloporphyrins [26]. Based on this information, there are no studies reported on the formation and observation of HER using CuPc incorporated on the MOF surface to prepare an effective electrocatalytic composite.

Therefore, this study reports on the synthesis, characterization and application of the Pd@CuPc/MOF composite for the hydrogen adsorption/desorption mechanisms through electrocatalytic route. Combining the merits of CuPc/MOF composites and hydrogen spillover mechanism, Pd-loaded CuPc/MOF hybrid composite was prepared in this contribution through simple impregnation method of CuPc and MOF followed by electroless Pd plating. This work can provide further insights into the properties of hybrid composites and the phenomenon of hydrogen spillover. To our knowledge, the synthesis and characterisations of Pd@CuPc/MOF hybrid composite was not reported to date. The MOF (HKUST-1) was prepared following the hydrothermal method, which allows precise control over the size, shape distribution, highly crystalline solid, efficient synthetic conditions and ability to control the morphology of this material [26]. Unlike high uncertainty of the MOF bridging technique, electroless Pd plating of CuPc/MOF exhibits more controllable and reliable synthesis procedure. The resulting Pd@CuPc/MOF composite showed excellent structural and thermal stability as well as significant activity as an electrocatalyst for HER application in acidic medium.

2. Experimental

2.1. Materials

Copper nitrate trihydrate ($Cu(NO_3)_2 \cdot 3H_2O$), trimesic acid (H_3BTC), sodium hypophosphite ($NaPO_2H_2$) and tetrabutylammonium percholate (TBAP) were purchased from Sigma Aldrich, South Africa. Phthalimide, 32% hydrochloric acid (HCl), methanol, nitrobenzene, copper nitrate, dimethylformamide (DMF), sodium hydroxide (NaOH), 25% ammonia solution (NH_4OH), Ammonium chloride (NH_4Cl), ethanol (EtOH), dimethyl sulfoxide (DMSO), 99% palladium chloride ($PdCl_2$) and sulphuric acid (H_2SO_4) were purchased Rochelle chemicals. Ammonium heptamolybdate ($(NH_4)_6Mo_7O_{24}$), and urea (CH_4N_2O) were purchased from uniLAB. Unless otherwise mentioned, all reactants were used as purchased without further purification. Electrochemical measurements were carried out at 22 ± 2 °C.

2.2. Synthesis

CuPc was synthesized from phthalimide according reported method for phthalocyanine dye preparation [27]. MOF was synthesized by following a hydrothermal procedure [28]. CuPc/MOF composite was prepared by simple impregnation method of CuPc

and MOF. Approximately, 0.1 g of as-synthesized MOF sample was dehydrated at 150 °C for 1 h, and then suspended in 10 mL DMF. An appropriate amount of 1.4 mL of CuPc solution in DMF (0.06 mol. L^{-1}) was added to the suspension of MOF solution and the mixture solution was then stirred magnetically for 24 h at room temperature. The product was recovered by filtration and washed with ethanol and then dried overnight at 50 °C. Pd@MOF and Pd@CuPc/MOF (Scheme 1) were prepared by electroless Pd plating method [29] of CuPc/MOF composite. Briefly, the plating solution was prepared by initially dissolving 1 g of $PdCl_2$ in 2.0 mL of 32% HCl and 10 mL of ultra-pure water, then heated at 50 °C for 30 min with constant stirring at 300 rpm. After complete dissolution of $PdCl_2$, 80 mL of 28% NH_4OH and 27 g of NH_4Cl were added respectively. The mixture was then transferred to 500 mL volumetric flask and made up to the mark with ultra-pure water. The electroless plating bath, containing 25 mL of 5 $g.L^{-1}$ of sodium hypophosphite as reducing agent to initiate the reaction and 2.5 g batch of MOF or CuPc/MOF composite was subjected to constant agitation (300 rpm) for 30 min at 50 °C in a separate bath to avoid decomposition during storage of the bath. Finally, the 25 mL of plating solution was added into the bath solution and the mixture was agitated for 30 min to allow the plating of Pd to the surface of the composite. The mixture was filtered, washed with ultra-pure water and dried for overnight at 80 °C.

2.3. Materials characterization

Optical absorption spectra were recorded at room temperature in the wavelength region 200–800 nm using a Varian Cary 300 UV–Vis–NIR spectrophotometer. The structure of CuPc, MOF and CuPc/MOF composite was analyzed using X-ray diffraction (XRD Phillips PW 1830, CuK_α radiation, $\lambda = 1.5406$ A). The formation of the composite was confirmed by Cary 600 series Fourier transform infrared (FTIR) spectrometer (Spectrum II PerkinElmer). The spectra were obtained at room temperature in the wave number range between 400 and 4500 cm^{-1}. A minimum of 32 scans were collected at a resolution of 4 cm^{-1}. Morphological characterizations were performed using field emission scanning electron microscopy (FE-SEM, Auriga® Carl Zeiss) operated at a voltage of 30 kV coupled with EDS detector for elemental analysis. The thermal stability of the samples was performed on a PerkinElmer STA 6000 instrument connected to a PolyScience digital temperature controller under N_2 gas purged at a flow rate of 20 $mL.min^{-1}$. The calibration of the instrument was performed using indium (m.p. 156.6 °C) and aluminium (m.p. 660 °C). Samples ranging between 1 and 4 mg were heated from 30 to 600 °C at a constant heating rate of 10 °C min^{-1}. The data was collected and analyzed using Pyris software®.

Low-pressure nitrogen (77 K) adsorption isotherms were performed using an ASAP2020 instrument (Micromeritics). Approximately, 300 mg of MOF and composites were heated to 180 °C with a rate of 2 °C.min^{-1} and outgassed at 180 °C for 24 h.

Electrochemical measurements were carried out using EPSILON electrochemical workstation. The data was collected using a conventional three-electrode set-up with gold electrode (3 mm diameter, 0.071 cm^2 area) as a working electrode, Pt wire as a counter electrode and Ag/AgCl as a reference electrode. Repetitive scanning of the solutions of MOF, Pd@MOF and CuPc/MOF composite (~2.0×10^{-4} $mol.L^{-1}$) was measured from −2.0–1.25 V at the scan rate of 0.02–0.10 Vs^{-1}. Electrochemical experiments were performed in 10 mL of 0.1 M TBAP/DMSO electrolytic system. HER studies were done using different concentrations of 0.03–0.45 $mol.L^{-1}$ H_2SO_4 as H_2 source in 0.1 $mol.L^{-1}$ TBAP/DMSO system and ~2.0×10^{-4} $mol.L^{-1}$ of CuPc, MOF and CuPc/MOF composite as electrocatalysts.

3. Results and discussion

3.1. Structural properties

Fig. 1 shows the comparative UV–Vis absorption spectra for the Pd@CuPc/MOF hybrids, Pd@MOF and MOF in H_2SO_4 solution. The spectra of MOF and Pd@MOF in H_2SO_4 showed no absorption in the

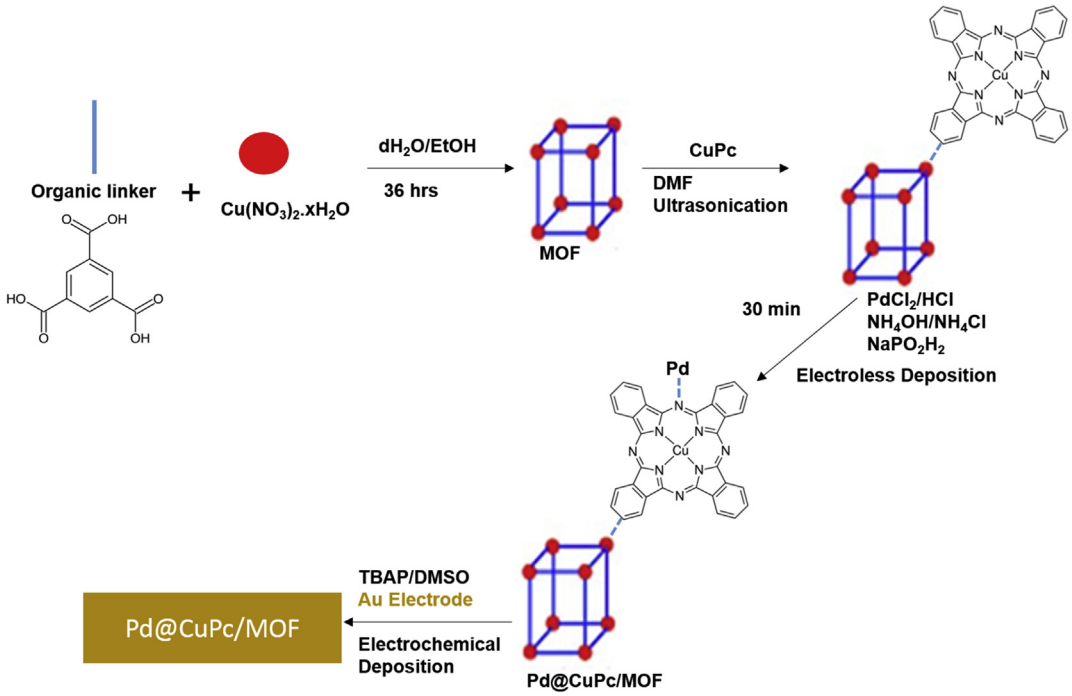

Scheme 1. Preparation of Pd@CuPc/MOF through simple impregnation method of CuPc and MOF in DMF followed by electroless Pd plating.

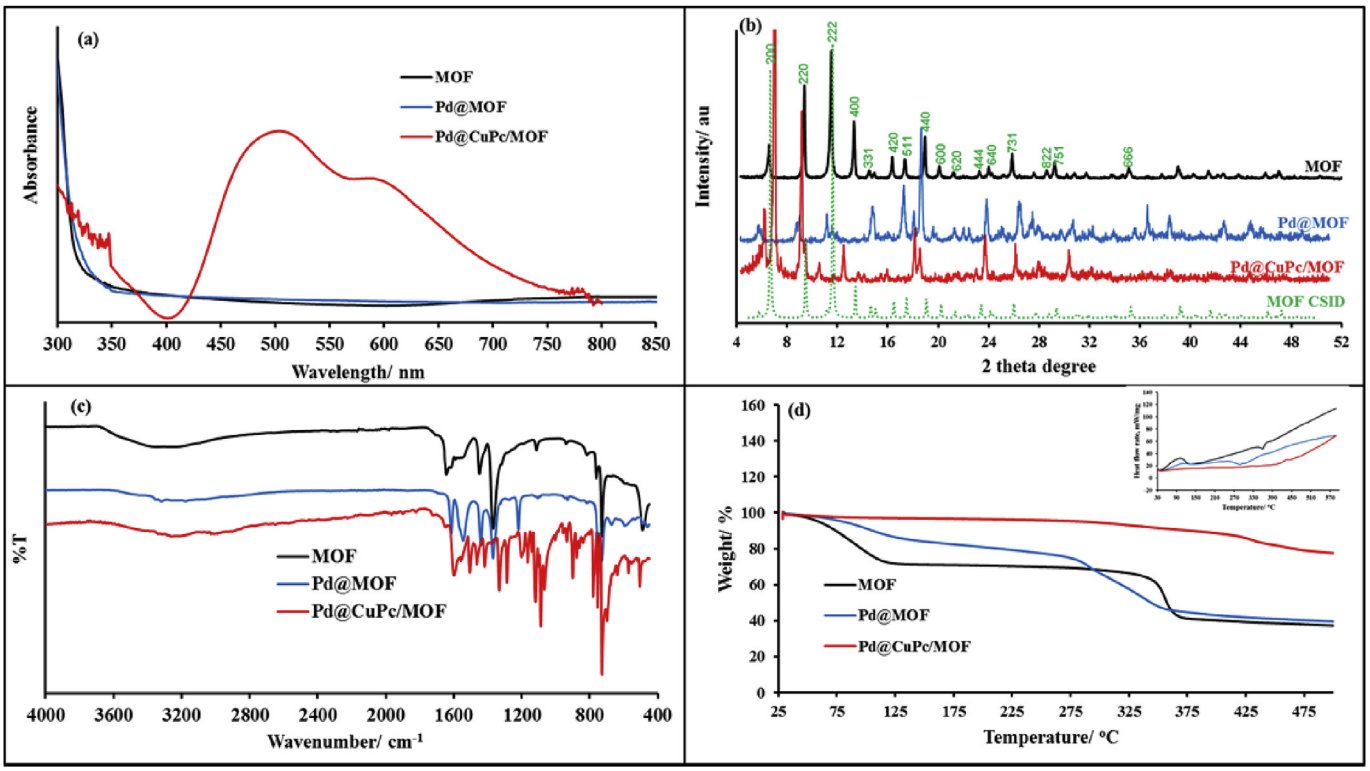

Figure 1. (a) UV–vis spectra (in 2 ppm H_2SO_4); (b) XRD patterns; (c) FTIR spectra; and (d) TGA curves of MOF, Pd@MOF and Pd@CuPc/MOF composite. Inset DSC curves.

ultra-visible region due to the instability of MOF structure in concentrated acid [30]. The UV–Vis spectrum of phthalocyanines originates from molecular orbitals within the aromatic 18π electron system [31] and they have been considered as electrophotographic materials due to their absorption ability in the ultraviolet and visible region [32]. The evidence for the successful electroless Pd deposition onto CuPc/MOF is demonstrated by the change in the absorption bands as shown in Fig. 1(a). For example, CuPc showed absorption peaks at 798 (Q band) and 370 nm (B band) in concentration H_2SO_4 owing to insolubility of unsubstituted CuPc in most organic solvents [33]. The broadening of B band was observed due to the superimposition of the B1 and B2 bands in 300–400 nm regions, which progress to monomers leading to aggregates [22]. However, after the phthalocyanine was incorporated with MOF and followed by deposited Pd nanoparticle, there was a blue shift and broadening in absorption peak confirming formation attachment of Pd nanoparticles on CuPc in the composite.

Fig. 1(b) shows X-ray diffraction (XRD) patterns of MOF, Pd@MOF and Pd@CuPc/MOF composite. The XRD pattern of MOF was agreement with that reported in the literature [35,36], demonstrating a successful synthesis procedure. The peaks shown in Fig. 1(b) of MOF pattern, appeared at small 2θ angles are characteristics of microporous materials, which possess numerous tiny pores or cavities that are in accordance with typical MOF structure [36]. The XRD pattern of Pd@CuPc/MOF (Fig. 1(b)) shows the peak at $2\theta = 6.97^{o}$ corresponding to reflection (110) of CuPc. The pattern of copper phthalocyanine was reported [31], and has the most intense peaks at $2\theta = 5.7$, 6.9 and 9.1^{o} corresponding to miller indices (111), (110) and (111), respectively [34]. It is interesting to notice that the diffraction patterns of both composites were similar to that observed for the parent MOF, indicating that the well-defined MOF structure has been preserved and the incorporation of Pd and CuPc component did not prevent the formation of linkages between copper dimers and BTC bridges. Furthermore, the reduction of intensity observed in Pd@CuPc/MOF is related to the low crystallization caused by the incorporation of CuPc [14]. On one hand, the CuPc component suspended in the reaction mixture may act as a nucleation surface, promoting the formation of very small MOF crystallites, as supported by the observed intense peak of CuPc in the composite. On the other hand, reduction of some diffraction peak intensities was also due to incorporation of Pd resulting in slight change of the structural regularities of MOF and CuPc after loading palladium. This was supported by XRD pattern of Pd@MOF alone. Furthermore, palladium coated materials showed two reflection indexes of (111) and (200) at 39 and 45^{o} angle 2theta, respectively, and were identified by the cubic phase of Pd (card 05-0681 in the JCPDS file).

Fig. 1(c) presents the FTIR spectra of MOF, Pd@MOF; and Pd@CuPc/MOF composite. The FTIR spectrum of CuPc has been described in detail elsewhere [37,38]. As shown in Fig. 1(c), all intense band around 1489 cm^{-1} were due to phenyl modes in MOF structure. Since MOF consisted of benzene-1,3,5-tricarboxylic acid (H_3BTC), bands of the spectrum essentially derived from H_3BTC and it was shown that the band at 1374 cm^{-1} was assigned to C–O of H_3BTC [39,40]. The bands at 1450 and 1566 cm^{-1} were attributed to C=O of H_3BTC and the one at 1646 cm^{-1} resulted from aromatic C=C and 1718 cm^{-1} from COO–of H_3BTC [39,40]. In case of Pd@MOF, the most direct evidence was the appearance of the bands at 1546, 1200 cm^{-1} and the weaker band at 670 cm^{-1} (see Fig. 1(c)), which could ascribe to COO– and C–O due to the COO– bonded to coated Pd on the surface of MOF. The similar behaviour was observed in Pd@CuPc/MOF. The incorporation of palladium nanoparticles resulted in change in the shape and frequencies of the bands in this region, indicating that carboxylic group are involved in the attachment of Pd with the CuPc/MOF surface.

Fig. 1(d) demonstrates TGA and DSC curves of MOF, Pd@MOF and Pd@CuPc/MOF composite. At the initial stage MOF and Pd@MOF, degradation step is observed due to the evaporation of

water and removal of all organic material, including the evaporation of guest molecules from the pores such as solvent ethanol [41]. Between 100 and 360 °C, the weight loss was almost linear in both MOF and Pd@MOF indicating the high thermal stability of the MOF. These TGA profiles agreed very well with that of MOF originally reported by Azhar et al. [42]. A sudden degradation change (around 40 wt%) was observed at 365 °C due to the loss of BTC linker and the remaining product was reported to be CuO [41]. Furthermore, there was improvement of thermal stability upon introduction of Pd on MOF surface. In the case of Pd@CuPc/MOF, the thermal stability improved due to the presence of CuPc which is known to have high thermal stability [34,43]. The MOF composite maintained its structure up to 400 °C and after that a sudden weight loss was observed, which was attributed to decomposition of the composite.

The inset in Fig. 1(d) presents DSC curve of MOF, Pd@MOF, and Pd@CuPc/MOF composite. In these results, both recrystallization and melting transitions which corresponds to exothermal and endothermal processes were observed due to the fact that MOF decomposes completely to its starting materials at high temperatures. With the DSC results, we defined the end of the first ramp as a dry state where no water is adsorbed in the MOF that confirm moisture instability of this MOF [41]. As shown in Fig. 1(d) inset, the MOF and Pd@MOF have distinctly higher heat flow rates associated with latent heat compared to the Pd@CuPc/MOF, which were associated with sensible heat [44].

3.2. Morphological analysis

The FE-SEM microphotographs (Fig. 2) were used to investigate the morphologies and microstructures of MOF, Pd@MOF and Pd@CuPc/MOF composite. As shown in Fig. 2(a), a typical irregular crystal with octahedral shapes were observed in MOF as indicative of a low control on the crystal growth parameters [45]. The EDS (Fig. 2(b)) showed the presences of C—, O— and Cu—atoms as the elemental composition in the MOF structure. The inset image of Fig. 2(a) shows that MOF crystals at 5 KX magnifications and 1 μm scale, have smooth surfaces. This observation confirmed that hydrothermal synthesis gives pure, highly crystalline MOF materials. The SEM images of Pd@MOF in Fig. 2(c) and (e) show similar octahedral shapes with the presence of spherical crystals which can be attributed to morphologies of CuPc. Magnification of the octahedral crystals (inset images in Fig. 2(c) and e) of Pd@MOF composites showed that after introduction of Pd, the structure of the crystals develops rough surfaces which can be due to interaction of Pd on the material surface. Clear demonstration of rough surfaces is observed when the Pd is introduced on CuPc/MOF composite in which the inset image (Fig. 2(e)) shows the interconnecting structures of nanoparticles on the surfaces of CuPc/MOF composite. This confirms that there is an interaction between CuPc/MOF and Pd nanoparticles due to extra lone pair of electrons provided by CuPc in the composite. EDS results of MOF and its composites (Fig. 2(d) and f) also revealed the presence of copper, carbon, oxygen and deposited Pd. Furthermore, the EDS analysis of composites showed the presence of chloride and sulphur which are due to chemical reagent used during the synthesis. It is noticeable that this intensity peak of Cu atom decreased in the composite of Pd@CuPc/MOF (Fig. 2(f)). The diminution of this peak is attributable to the strong interaction between the two components and presence of CuPc. This observation is in good consent with the XRD results.

3.3. Gas absorption properties

Porosity is an important parameter that has effect on gas adsorption. Results of surface area and porous structure obtained from nitrogen adsorption measurements are listed in Table 1 and Fig. 3. The surface properties of materials were evaluated from nitrogen adsorption measurements at 77 K (Fig. 3). The parent material MOF exhibits a Type-I isotherm with a small hysteresis loop at relative pressure from 0.81, indicating the predominant microporous and mesoporous character of such material [46]. The loops found for both composites (Pd@MOF, Pd@CuPc/MOF) might be caused by the larger pores between composites particles. Table 1 shows that the surface area of 817.54 m^2g^{-1} for MOF is in the range of values reported previously [47]. The surface area values of composites decrease to 58.22 and 241.54 m^2g^{-1} in Pd@MOF and Pd@CuPc/MOF, respectively. As shown in Table 1, the reduction in surface area and pore volume of the composites can be ascribed to the following facts: 1) the pore volumes of the composites are decreased by introduction of Pd and CuPc with much low porosity; 2) the introduction of excessive Pd and CuPc caused low crystallization of products, which has been confirmed by decreased intensities of XRD peaks for Pd@MOF and Pd@CuPc/MOF; and 3) Pd and CuPc in the composite remain as agglomerates as observed in SEM images, which caused the obvious reduction of the total pore volume of 0.109 cm^3g^{-1}, compared to 0.312 cm^3g^{-1} of MOF. Furthermore, the V_{mic}/V_{pore} ratio of samples decreases from 0.769 (MOF) to 0.0086 (Pd@MOF) as indicative of Pd being trapped in the pores of MOF crystal structure. In case of Pd@CuPc/MOF, the ratio observed (0.709) is closer to that of MOF. This shows that the Pd is attached to CuPc support.

3.4. Electrochemical characterization

3.4.1. Electrodeposition

The electrodeposition of MOF, Pd@MOF and Pd@CuPc/MOF composite on gold electrode was achieved in 0.1 M TBAP/DMSO electrolytic system by sweeping the potentials in the range −0.2–1.25 V for 10 cycles at a scan rate of 0.05 Vs^{-1}. During electrodeposition, the cyclic voltammograms (CVs) were recorded simultaneously to monitor the deposition process. A typical CV of MOF, Pd@MOFand Pd@CuPc/MOF deposition is illustrated in Fig. 4(a–c), respectively, showing the deposition growth which arises from the material to the surface of working electrode.

The deposited materials (Fig. 4(a-c)) demonstrated double redox reversible peaks at $E_{p,c}$~ 0.61 V and $E_{p,a}$~ −0.64 V (peak I) which are attributed to diffusion of electrons [26] of the deposited material. Second redox reversible peaks (peak II) are observed at $E_{p,c}$~0.22 V which is due to reduction reaction of $[Cu_3(BTC)_2 \rightarrow Cu_3(BTC)_2^-]$ and at Ep,a~0.25 V attributed to reverse oxidation reaction of $[Cu_3(BTC)_2^- \rightarrow Cu_3(BTC)_2]$ [26]. The Faradaic contributions (redox process) onto gold electrode (blank) was observed between −0.550 and −0.770 V (peak III) which is a typical redox process of bare Au electrode [48]. The irreversible cathodic peak (peak IV) was observed at around −1.65 V in all materials. With an increase in cycle number, intensity of oxidation/reduction peaks increased that confirm growth on the electrode [49]. However, it was noticeable that the introduction of Pd nanoparticle on the surface of MOF (Fig. 4(b)) resulted in the reduction of electrodeposition growth. On the other hand, with the presence of CuPc, the improvement of current density was observed as compared to Pd@MOF composite. Furthermore, there was shift in the redox peak to more negative potential in the Pd@CuPc/MOF composite (Fig. 4(c)) as an indication that the CuPc structure is conductive and the diffusion of electrons along the MOF framework was taking place [50].

3.5. Scan rate dependent

Fig. 5(a) shows the cyclic voltammograms of a MOF, Pd@MOF, and Pd@CuPc/MOF modified electrode and an unmodified Au electrode immersed in 0.1 M TBAP/DMSO electrolytic solution at

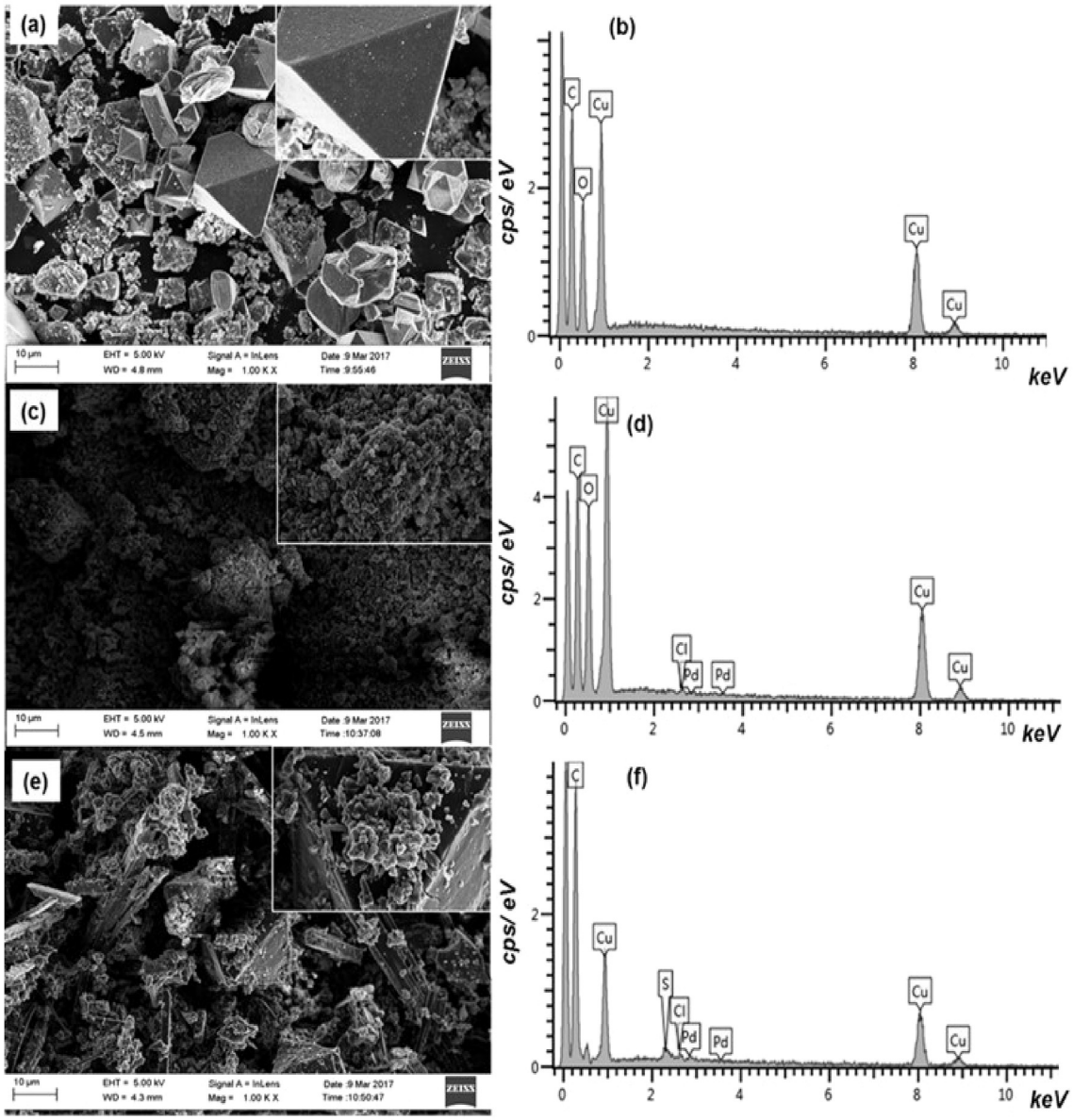

Figure 2. SEM image of (a) parent MOF, (c) Pd@MOF (e) Pd@CuPc/MOF composite (inset:5 kX magnification on the crystal structure to view the surface of the crystal at 1 μm) and EDS spectrum of (b) MOF, (d) Pd@MOF, (f) Pd@CuPc/MOF composite.

0.10 Vs^{-1}. For MOF, a prominent reduction peak was recorded at around −0.783 V vs Ag/AgCl followed by a well-defined stripping anodic peak at −0.653 V. The development of new reduction peak was observed at more negative potential (~-1.64 V) without its corresponding anodic coupling counterpart [51]. This response differs significantly from that recorded bare electrode in solution with several appearances of oxidation peaks at 0.652 and 1.03 V.

Introduction of Pd on the MOF surface showed reduction peak at

Table 1
Parameters of the surface area and porous structure for MOF, Pd@MOF and Pd@CuPc/MOF composite

Material	S_{BET} (m^2/g)	$S_{Langmuir}$ (m^2/g)	V_{pore} (cm^3/g)	V_{mic}/V_{pore}
MOF	614.668	817.548	0.312	0.769
Pd@MOF	42.205	58.230	0.153	0.009
Pd@CuPc/MOF	183.168	241.541	0.110	0.709

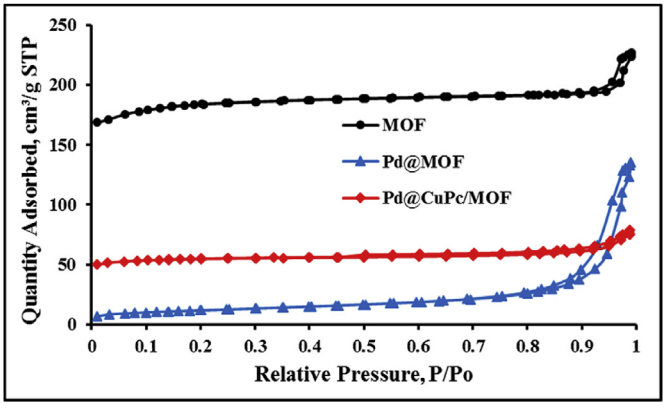

Figure 3. Nitrogen adsorption isotherms of MOF, Pd@MOF, and Pd@CuPc/MOF composite at 77 K.

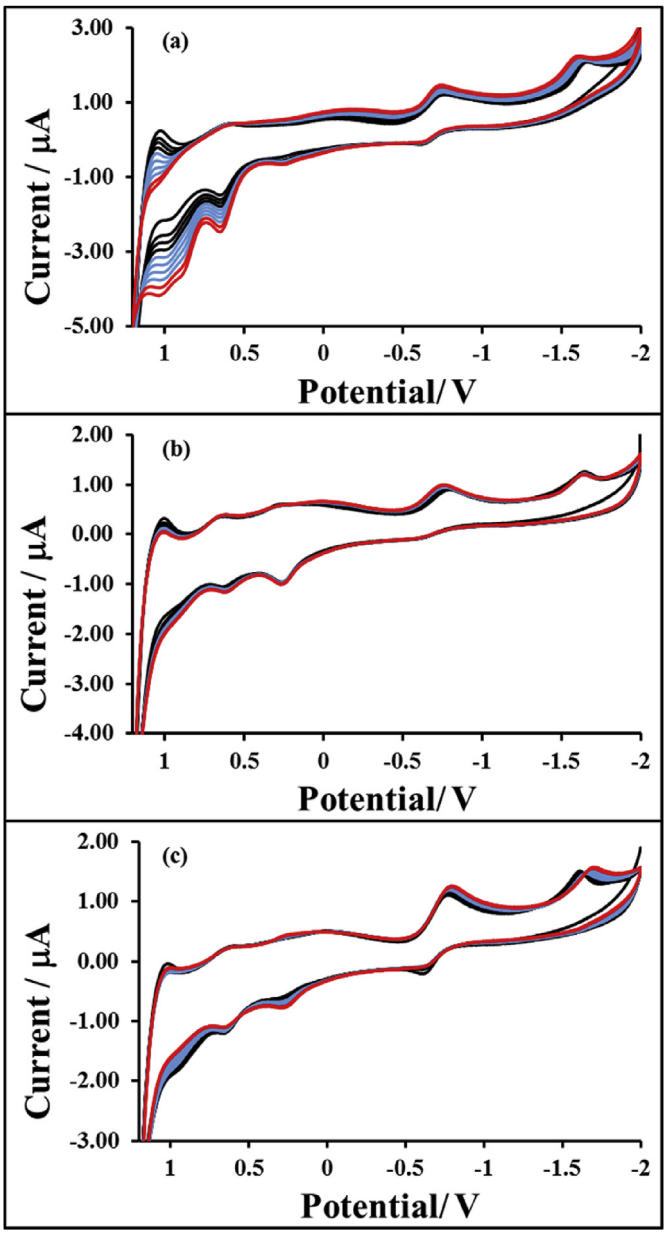

Figure 4. Electrodeposition of MOF, Pd@MOF and Pd@CuPc/MOF in 0.1 M TBAP/DMSO electrolytic system in the range −0.2–1.25 V for 10 cycles at a scan rate of 0.05 Vs^{-1} using a gold working electrode.

0.585 V vs Ag/AgCl coupled with a stripping oxidation peak at 0.607 V. This peak is associated with the oxidation of electrochemically formed palladium metal present on the MOF surface. As can be seen in Fig. 5(a), the CV response of Pd@CuPc/MOF consists of three cathodic peaks at ~ 0.674, 0.232, and −0.830 with corresponding anodic peaks at ~0.638, 0.269 and −1.10 V as indicative of redox species in the composite. These redox couples appeared at more negative potential as compared to neat MOF and Pd@MOF materials. However, irreversible reduction peak was also observed at around −1.81 V. The irreversible reduction peak at more negative potential, which shows that the composite is a suitable electrocatalyst [51]. To further evaluate the electrochemical activities of coated MOF, Pd@MOF and Pd@CuPc/MOF composite on the working electrode, cyclic voltammetry in 0.1 M TBAP/DMSO electrode system at different scan rate (0.02–0.10 Vs^{-1}) is used and results are presented in Fig. 5(b–d). For all the materials, the anodic-cathodic wave separations increased with increasing scan rates which in an evident of diffusion-controlled reactions on the surface of the materials [51,56]. Multiscan voltammogram of composites shows triple redox reversible peaks at $E_{p,c}$ ~ −0.80 and $E_{p,a}$~ −1.10 V which are attributed to gold electrode [50] and second and redox couples at $E_{p,c}$~ 0.23 and $E_{p,a}$~0.27 V; and $E_{p,c}$~ 0.67 and $E_{p,a}$~0.64 V and which is due to diffusion of electrons among Pd nanoparticle to MOF material. The plot of logarithm of the current against the logarithm of the scan rate was constructed for each material and is represented in Fig. 6(a). A linear relationship was observed with the slopes were 0.310, 0.385 and 0.308 for MOF, Pd@MOF and Pd@CuPc/MOF materials, respectively. These results show that all materials exhibit the characteristics of a response due to diffusion transport of electron [50,52,53]. Furthermore, these observations were supported by the influence of the square root of scan rate on the peak current showed a linear relationship in the range of 0.02–0.10 Vs^{-1} (Fig. 6 b) which is of a typical diffusion controlled process [26,54].

The diffusion coefficient, *D*, was determined for catalysts using cyclic voltammetry and following the Randles-Ševćik equation (Eq. (4)) for a quasi-reversible system [53,55].

$$Ip = (2.65 \times 10^5)\, n^{3/2} A C D^{1/2} v^{1/2} \quad (4)$$

where, *n* is the number of electrons transferred, *A* is the electrode area in cm^2, *D* is the diffusion coefficient in $cm^2\ s^{-1}$, *C* is the bulk molar concentration of the electroactive species in $mol.cm^{-3}$ and *v* is scan rate is Vs^{-1}. The diffusion coefficients were determined to be 1.48×10^{-6}, 0.88×10^{-6} and 0.99×10^{-6} $cm^2 s^{-1}$ for MOF, Pd@MOF and Pd@CuPc/MOF materials, respectively.

3.6. Hydrogen studies

Electrocatalytic studies of MOF and its derivative composites were performed in TBAP/DMSO electrolyte with addition of 0.300 $mol.L^{-1}$ H_2SO_4 as a hydrogen source and the results are shown in Fig. 7(a). The HER studies of MOF at different concentrations and scan rates are shown in Fig. S4, where the based performance was obtained at 0.300 $mol.L^{-1}$ H_2SO_4 and 100 $mV.s^{-1}$. According to the results, H_2SO_4 gives hydrogen reduction peak around −1.0 V in absence of catalysts which indicates the ability of Au electrode to adsorb some of the proton. In the case of fabricated MOF electrode, the emerged reduction waves correspond to the hydrogen evolution reaction [26]. Furthermore, two couples of cathodic and anodic peaks, respectively labeled B_1/A_1 and B_2/A_2 (Fig. 7(a), inset) relate to different hydrogen sorption processes in the MOF material. Voltammogram of Pd@MOF upon addition of acid shows similar behaviour with less current response as compared to MOF. The decrease in current was attributed to the presence of Pd nanoparticles as an indication of hydrogen spillover mechanism. It is known that hydrogen usually combines with Pd to form Pd hydride instead of physically adsorbing on Pd surfaces [26,54-56]. The similar behaviour was observed in Pd@CuPc/MOF, however, the HER process was better than the one of Pd@MOF without affecting the hydrogen desorption and adsorption. The results were due to the oxidation of H_2 remaining in the vicinity of MOF particles due to slow diffusion in the CuPc matrix. It is important to note that the hydrogen absorption and H_2 evolution signals are very well separated [51]. It is clear that matrix side effects like H_2 trapping, often leading to overlapping peaks and thus to an overestimation of the β phase composition [51]. As it is well known, the Tafel slope is an important parameter to depict the relationship between the overpotentials and the exchange current density during HER, which is used to further evaluate the catalytic ability [57-59].

Fig. 7(b) shows Tafel plots (V versus log i_o plots) for blank

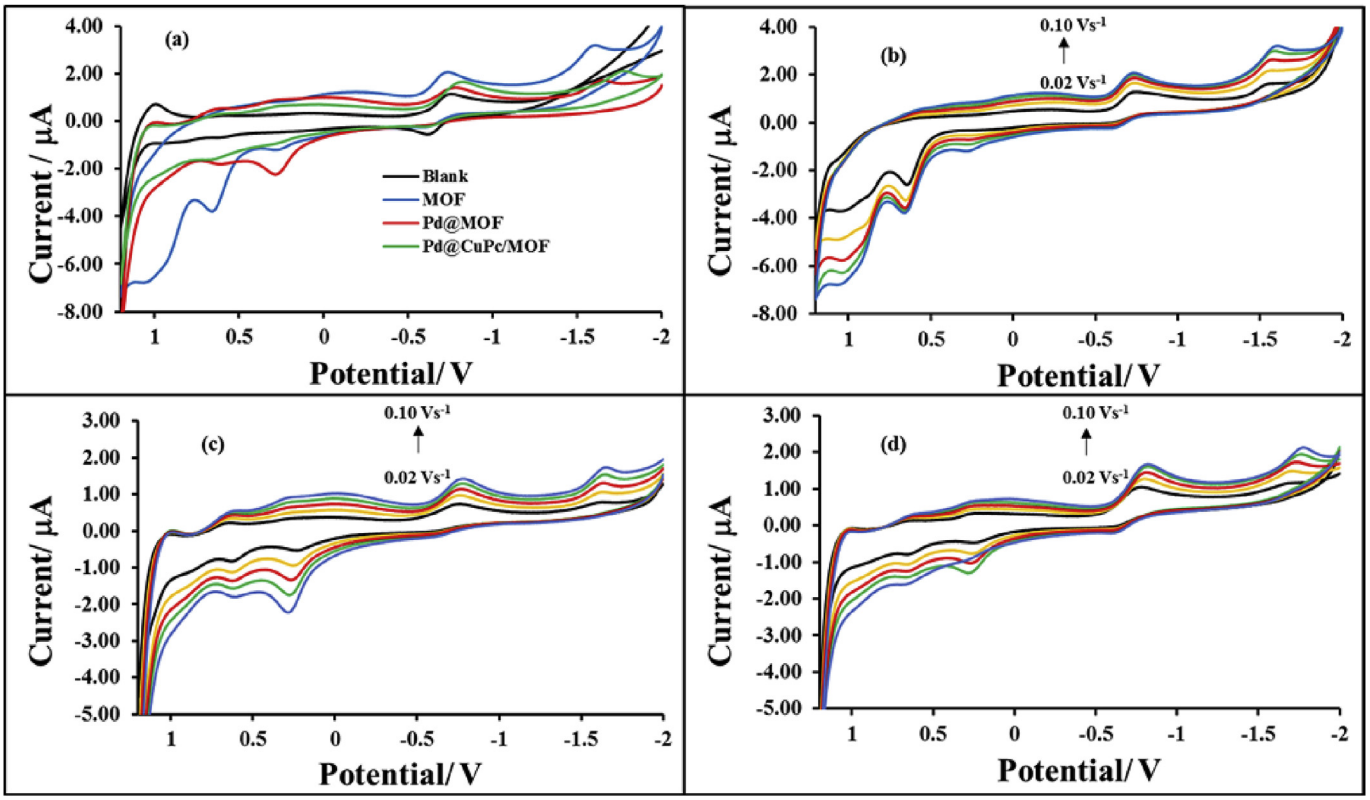

Figure 5. Cyclic voltammetric curves of (a) Blank, MOF, Pd@MOF and Pd@CuPc/MOF at 0.10 Vs^{-1}; (b) MOF, (c) Pd@MOF and (d) Pd@CuPc/MOF composite (~2.0 × 10^{-4} $mol.L^{-1}$) in 0.1 M TBAP/DMSO electrolytic system at different scan rate (0.02–0.10 Vs^{-1}).

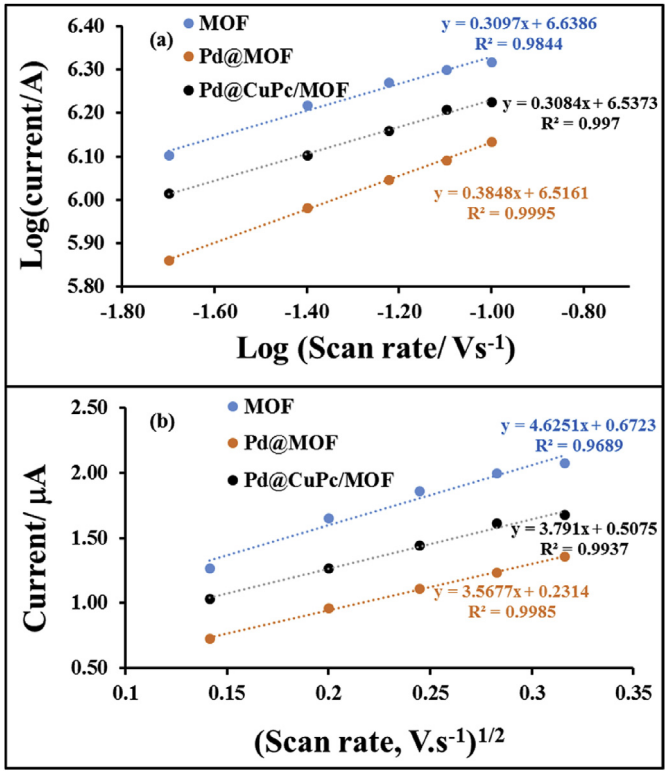

Figure 6. (a) The log-log plot of the absolute value of the peak current vs scan rate and (b) Peak current as a function of square root of scan rate for MOF, Pd@MOF and Pd@CuPc/MOF composite in 0.1 M DMSO/TBAP electrolytic system at different scan rate (0.02–0.10 Vs^{-1}).

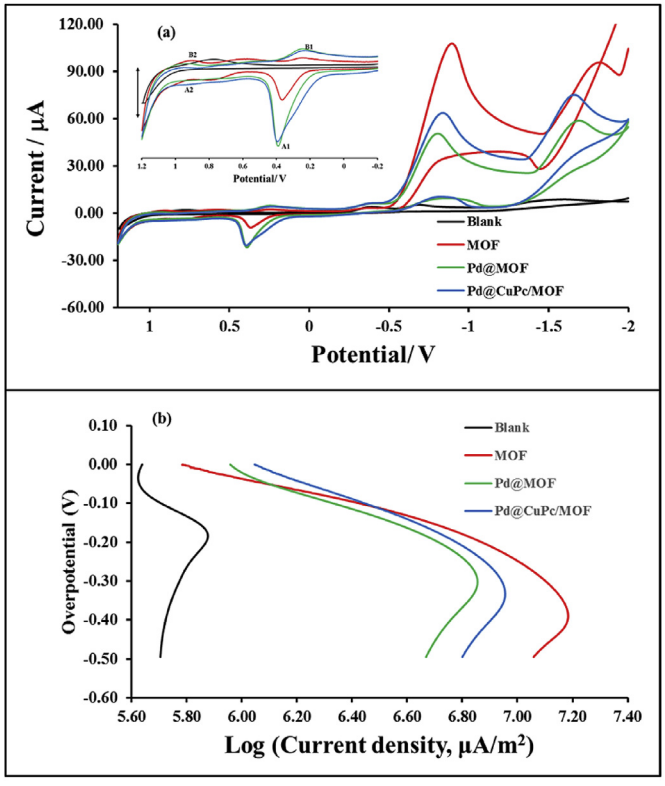

Figure 7. (a) CV and (b) Tafel plots curves of blank, MOF, Pd@MOF and Pd@CuPc/MOF composite (~2.0 × 10^{-4} $mol.L^{-1}$) at 0.10 Vs^{-1} (Inset: CV enlargement at the selected area) in the presence 0.300 $mol.L^{-1}$ H_2SO_4 on Au electrode in 0.1 $mol.L^{-1}$ TBAP/DMSO electrolytic system.

Table 2
Experimental values of Tafel slope (b), charge transfer coefficient ($1-\alpha$) and exchange current density (i_0) of blank, MOF, Pd@CuPc, Pd@MOF and Pd@CuPc/MOF composite

Material	H_2SO_4 (mol.L^{-1})	Slope (b) (V.dec^{-1})	-b (mV.dec^{-1})	1-α	logi_0 (μA.m^{-2})	i_0 (A.m^{-2})
Blank	0.033	−0.4593	459.3	0.1288	5.88	0.759
	0.150	−0.4714	471.4	0.1255	5.88	0.759
MOF	0.033	−0.3208	320.8	0.1844	5.93	0.851
	0.075	−0.3277	327.7	0.1805	6.22	1.660
	0.150	−0.1319	131.9	0.4484	6.39	2.455
	0.300	−0.2367	236.7	0.2499	6.70	5.012
Pd@CuPc[a]	0.033	−0.110	105.9	0.560	7.10	12.59
	0.075	−0.170	171.1	0.350	7.30	19.95
	0.150	−0.140	137.0	0.430	7.00	10.00
	0.300	−0.180	184.2	0.32	7.42	26.30
Pd@MOF	0.300	−0.1927	192.7	0.307	6.90	7.100
Pd@CuPc/MOF	0.300	−0.1769	176.9	0.334	7.00	8.900
PABA/MOF [50]	0.300	−0.1305	130.5	0.45	1.55	35.48
MOF-3wt%-PABA [26]	0.300	−0.1667	166.7	0.355	1.50	31.62
Cu-Pt-NPCC [28]	0.500	[b]	[b]	0.330	−2.62	0.002
MOF-$CoSe_2$ [20]		0.042	42	0.328	[b]	[b]

a = HER studies at −1.5 V
b = no reported literature value,

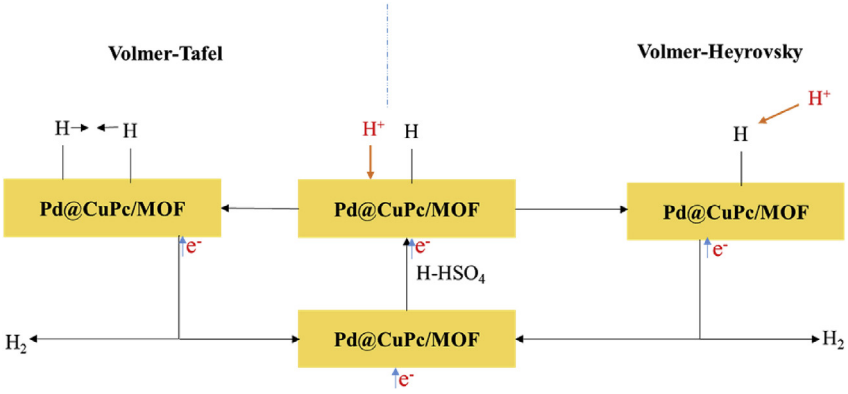

Scheme 2. Mechanisms for hydrogen evolution reaction using Pd@CuPc/MOF composite (~2.0 × 10^{-4} mol.L^{-1}) at 0.10 Vs^{-1} in the presence 0.300 mol.L^{-1} H_2SO_4 and 0.1 mol.L^{-1} TBAP/DMSO electrolytic system on Au electrode.

electrode, MOF, Pd@ MOF and Pd@CuPc/MOF materials which reveal the kinetics of HER process. The HER processes are demonstrated by three major reaction steps, thus adsorption step (Volmer reaction), electrochemical discharge (Heyrovsky reaction) and combination step of adsorbed hydrogen (Tafel reaction) in acid solution [52]. Table 2 shows the Tafel slope of Pd@CuPc/MOF with the value of 176.9 mVdec^{-1}, which is much smaller than those of Pd@MOF (192.7 mVdec^{-1}) and MOF (220.6 mVdec^{-1}). Such high values have already been reported in the literature on b range from 171 mV/dec (for CPE/H-IL@Pd 10%) to 279mV/dec (for CPE) [52]. In comparison, Pd@CuPc (Fig. S4) was investigated at different concentration and there was no observation of HER cathodic peak at around −0.5 V as obtain in MOF and its derivatives. However, it was seen that Pd@CuPc undergoes hydrogen evolution reaction at −1.5 V and the resulted Tafel parameters are also tabulated in Table 2.

It means the lower electron transfer resistivity, revealing that HER occurred here follows the Volmer reaction coupled with one of other two reactions of the mechanisms of Pd@CuPc/MOF during the catalytic process [26]. These values do not allow considering the Heyvrosky or Tafel mechanisms as the limiting steps (the values of b should be 40 mV/dec or 30 mV/dec respectively) [55]. This suggests that the Volmer reaction was the limiting step, despite higher values of b than expected (around 120 mV/dec). Therefore, the proposed mechanism for HER is shown in Scheme 2. In the Volmer-Heyrovsky mechanism, a proton from an acidic electrolyte layer reacts with one adsorbed hydrogen on the Pd@CuPc/MOF to form H_2 while in the Volmer-Tafel mechanism, two adsorbed surface hydrogens next to each other on the Pd@CuPc/MOF react to form H_2 molecule [7,8].

This observation is also supported by the charge transfer coefficient, α values (0.732, 0.693 and 0.676 for MOF, Pd@MOF and Pd@CuPc/MOF, respectively), which are all close to 0.5 [57]. These α values are similar to those reported in the literature as shown in Table 2 for Cu-Pt bimetallic nanoparticles supported metal organic framework-derived nanoporous carbon Cu-Pt-NPCC ($\alpha = 0.67$) [28], $\alpha = 0.55$ for PABA/MOF [50], $\alpha = 0.677$ for MOF-3.6 wt%PABA [26]; and $\alpha = 0.678$ for MOF-$CoSe_2$ [20]. In addition, the closer to 0.5 was primarily ascribed to the effective electron transport channels of the *Pc* and the increase of electro-chemically accessible surface area in nanocomposite materials, which was advantageous to facilitate the charge transfer at catalyst/electrolyte interface [53,55]. The values of exchange current density, i_o increase in an order of blank electrode (0.8 A.m^{-2}) < Pd@MOF (7.1 A.m^{-2}) < Pd@CuPc/MOF (8.9 A.m^{-2}) < MOF (15.1 A.m^{-2}) at low onset overpotential and 0.300 mol. L^{-1} H_2SO_4. It can be noticed that the surface area of our samples played a major role in improving the i_o values. The larger exchange current density indicates fast electron transfer rate and favourable HER kinetics [26,28].

4. Conclusions

In summary, an efficient electrocatalyst (Pd@CuPc/MOF) derived from CuPc and MOF was successfully synthesized through

impregnation procedure followed by electroless Pd deposition. The presence of CuPc on MOF surface was a crucial step for both the diffusion process of Pd atoms to form Pd@CuPc/MOF and the introduction of defects into CuPc to expose catalytic sites. The Pd@CuPc/MOF showed excellent HER activity with a low onset potential, Tafel slope of 176.9 mV dec^{-1}, high exchange current density (8.9 Am^{-2}) and robust stability in 0.300 $mol.L^{-1}$ H_2SO_4. Herein, the reported strategy of Pd@CuPc/MOF expose active sites of the MOF core, meanwhile, and maintain the porous carbon skeleton, which hold great potential for more applications in the electrocatalytic HER and hydrogen storage.

5. Compliance with ethical standards

The authors declare that they have no competing interests.

Acknowledgements

KDM and MJH are grateful to the National Research Foundation (Unique Grant Nos. 99166 and 99278) and University of Limpopo (Research Development Grants R202 and R232), South Africa for financial supports. We also acknowledge with great appreciation the Sasol Inzalo Foundation of South Africa for purchasing the STA instrument.

Appendix A. Supplementary data

Supplementary data related to this article can be found at https://doi.org/10.1016/j.renene.2017.11.084.

References

[1] Y. Ren, G.H. Chia, Z. Gao, Metal-organic frameworks in fuel cell technologies, Nano Today. 8 (2013) 577–587.
[2] S. Ehsan, M.A. Wahid, Hydrogen production from renewable and sustainable energy resources: promising green energy carrier for clean development, Renew. Sustain. Energy Rev. 7 (2016) 850–856.
[3] T. Wu, M. Pi, X. Wang, D. Zhang, S. Chen, Derived porous CoP3 concave polyhedrons as superior bifunctional electrocatalysts for the evolution of hydrogen and oxygen, Chem. Phys. 19 (2016) 2104–2110.
[4] A.A. Ensafi, M. Jafari-Asl, A. Nabiyan, B. Rezaei, M. Dinari, Hydrogen storage in hybrid of layered double hydroxides/reduced graphene oxide using spillover mechanism, Energy. 49 (2016) 103–114.
[5] N.K. Mahale, S.T. Ingle, Electrocatalytic hydrogen evolution reaction of nano-nickel decorated graphene electrode, Energy. 119 (2017), pp. 119:872-878.
[6] S. Bukola, B. Merzougi, S.E. Creager, M. Qamar, L.R. Pederson, N. Noui-Mehid Mohamed, Nanostructured cobalt-molybdenum carbides electrocatalysts for hydrogen evolution reaction, Int. J. Hydrogen Energy 41 (2016) 22899–22912.
[7] Q. Tang, D. Jiang, Mechanism of hydrogen evolution reaction on 1T-MoS_2 from first principles, ACS Catal. 6 (2016) 4953–4961.
[8] A.B. Laursen, A.S. Varela, F. Dionigi, H. Fanchiu, C. Miller, O.L. Trihammer, J. Rossmeis, S. Dahl, Electrochemical hydrogen evolution: sabatier's principle and the volcano plot, J. Chem. Edu. 89 (2012) 1595–1599.
[9] J.D. Benck, T.R. Hellstern, J. Kibsgaard, P. Chakthranont, T.F. Jaramillo, Catalyzing the hydrogen evolution reaction (HER) with molybdenum sulfide nanomaterials, ACS Catal. 4 (2014) 3957–3971.
[10] R. Ojani, R. Valiollahi, J.B. Raoof, Comparison between graphene supported Pt hollow nanospheres and graphene supported Pt solid nanoparticles for hydrogen evolution reaction, Energy. 74 (2014) 871–876.
[11] I. Hod, P. Deria, W. Bury, J.E. Modloch, C.W. Kung, M. So, M.D. Sampson, A.W. Peters, C.P. Kubiak, O.K. Farha, J.T. Hupp, A porous proton-relaying metal-organic framework material that accelerates electrochemical hydrogen evolution, Nat. Commun. 6 (2015) 8304–8312.
[12] M. Qamar, A. Adam, B. Merzougui, A. Helal, O. Abdulhamid, M.N. Siddiqui, Metal–organic framework-guided growth of Mo_2C embedded in mesoporous carbon as a high performance and stable electrocatalyst for the hydrogen evolution reaction, J. Mater. Chem. A 4 (2016) 16225–16232.
[13] L. Zhang, X. Chang, Z. Hu, L. Zhang, J. Shi, R. Gao, Selective solid phase extraction and preconcentration of mercury(II) from environmental and biological samples using nanometer silica functionalized by 2,6-pyridine dicarboxylic acid, Microchim. Acta 168 (2010), pp. 168:79-85.
[14] M. Zhao, S. Ou, C. Wu, Porous Metal–Organic frameworks for heterogeneous biomimetic catalysis, Chem. Res. 47 (2014) 1199–1207.
[15] M. Safari, Y. Yamini, M.Y. Masoomi, A. Morsali, A. Mani-Varnosfaderani, Magnetic metal-organic frameworks for the extraction of trace amounts of heavy metal ions prior to their determination by ICP-AES, Microchim. Acta 184 (2017) 1555–1564.
[16] Y. Zhao, Z. Song, X. Li, Q. Sun, N. Cheng, S. Lawes, Metal organic frameworks for energy storage and conversion, Energy Storage Mater. 2 (2016) 35–42.
[17] A.M. Fracaroli, H. Furukawa, M. Suzuki, M. Dodd, S. Okajima, O.M. Yaghi, Metal-organic frameworks with precisely designed interior for carbon dioxide capture in the presence of water, J. Am. Chem. Soc. 136 (2014) 8863–8866.
[18] Z.R. Herm, E.D. Bloch, R. Long, Hydrocarbon separations in metal–organic frameworks, Chem. Mater. 26 (2014) 323–328.
[19] S. Bhattacharjee, Y.L. Pillaiyar, P.S. Cho, Metal–organic frameworks for catalysis, Catal. Surv. Asia 19 (2015) 203–212.
[20] J. Lin, J. He, F. Qi, B. Zheng, X. Wang, B. Yu, K. Zhou, W. Zhang, Y. Li, Y. Chen, In-situ selenization of Co-based metal-organic frameworks as a highly efficient electrocatalyst for hydrogen evolution reaction, Electrochim. Acta 246 (2017) 258–264.
[21] J. Kim, S. Yeo, J.D. Jeon, S.Y. Kwak, Enhancement of hydrogen storage capacity and hydrostability of metal-organic frameworks (MOFs) with surface-loaded platinum nanoparticles and carbon black, Microporous Mesoporous Mater. 202 (2015) 8–15.
[22] H.W. Langmi, J. Ren, B. North, M. Mathe, D. Bessarabov, Hydrogen storage in metal-organic frameworks: a review, Electrochim. Acta. 128 (2013) 368–392.
[23] H. Zhou, J. Zhang, J. Zhang, X.F. Yan, X.P. Shen, A.H. Yuan, Spillover enhanced hydrogen storage in Pt-doped MOF/graphene oxide composite produced via an impregnation method, Inorg. Chem. Commun. 54 (2015) 54–56.
[24] Z. Wang, R.T. Yang, Enhanced hydrogen storage on Pt-doped carbon by plasma reduction, J. Phys. Chem. C 114 (2010) 5956–5963.
[25] Y. Li, R.T. Yang, Gas adsorption and storage in metal-organic framework MOF-177on and storage in metal-organic framework MOF-177, Langmuir. 23 (2007) 12937–12944.
[26] K.E. Ramohlola, M. Masikini, S.B. Mdluli, G.R. Monama, M.J. Hato, K.M. Molapo, E.I. Iwuoha, K.D. Modibane, Electrocatalytic hydrogen evolution reaction of metal organic frameworks decorated with poly (3-aminobenzoic acid), Electrochim. Acta 246 (2017) 1174–1182.
[27] D.K. Modibane, T. Nyokong, Synthesis, Photophysical and Photochemical Properties of Octa-substituted Antimony Phthalocyanines Polyhedron, 28, 2009, pp. 479–484.
[28] J.B. Raoof, S.R. Hosseini, R. Ojani, S. Mandegarzad, MOF-derived Cu/nano-porous carbon composite and its application for electro-catalysis of hydrogen evolution reaction, Energy. 90 (2015) 1075–1081.
[29] I. Ohno, Electroless deposition of palladium and platinum, Mod. Electroplat. (2010) 477–482.
[30] L. Fan, X. Zhang, W. Zhang, Y. Ding, W. Fan, L. Sun, Y. Panga, X. Zhao, Syntheses, crystal structures and UV-visible absorption properties of five metal-organic frameworks constructed from terphenyl-2,5,2′,5′- tetracarboxylic acid and bis(imidazole) bridging ligands, Dalt. Trans. 43 (2014) 6701–6710.
[31] P. Borker, A.V. Salker, Synthesis, characterization and photocatalytic studies of some metal phthalocyanines, Indian J. Chem. Technol. 13 (2006) 341–346.
[32] A.R. Gómez, L. Carlos, M.S. Hernández, I.F. Levin, J.A. Alatorre, J.C.A. Huitrón, M.E.S. Vergara, Optical absorption and visible photoluminescence from thin films of silicon phthalocyanine derivatives, Mater. (Basel). 6 (2014) 6585–6603.
[33] B. Köksoy, M. Durmuş, M. Bulut, Tetra- and octa-[4-(2-hydroxyethyl)phenoxy bearing novel metal-free and zinc(II) phthalocyanines: synthesis, characterization and investigation of photophysicochemical properties, J. Lumin. 161 (2015) 95–102.
[34] J. Sleven, C.G. Walrand, K. Binnemans, Synthesis, spectral and mesomorphic properties of octa-alkoxy substituted phthalocyanine ligands and lanthanide complexes, Mater. Sci. Eng. C 18 (2001) 229–238.
[35] G. Jia, Y. Gao, W. Zhang, H. Wang, Z. Cao, C. Li, J. Liu, Metal-organic frameworks as heterogeneous catalysts for electrocatalytic oxidative carbonylation of methanol to dimethyl carbonate, Electrochem. Commun. 34 (2013) 211–214.
[36] D.Y. Lee, D.V. Shinde, S.J. Yoon, K.N. Cho, W. Lee, N.K. Shrestha, S. Han, Cu-based metal – organic frameworks for photovoltaic application, J. Phys. Chem. C 118 (2013) 16328–16334.
[37] T. Wang, X.F. Zhang, X. Lu, Metal-free phthalocyanine aggregation and binding with amines: specific and general solvent effects on absorption and fluorescence properties, J. Mol. Struct. 1084 (2015) 319–325.
[38] D. Verma, R. Dash, K.S. Katti, D.L. Schulz, A.N. Caruso, Role of coordinated metal ions on the orientation of phthalocyanine based coatings, Spectrochim. Acta Part A Mol. Biomol. Spectrosc. 70 (2008) 1180–1186.
[39] B. Chen, S. Xiang, G. Qian, Metal-Organic Frameworks with functional pores for recognition of small molecules, Acc. Chem. Res. 43 (2010) 1115–1124.
[40] J. Kim, D.O. Kim, D.W. Kim, K. Sagong, Synthesis of MOF having hydroxyl functional side groups and optimization of activation process for the maximization of its BET surface area, J. Solid State Chem. 197 (2013) 261–265.
[41] A.R. Abbasi, M. Karimi, K. Daasbjerg, Efficient removal of crystal violet and methylene blue from wastewater by ultrasound nanoparticles Cu-MOF in comparison with mechanosynthesis method, Ultrason. Sonochem. 37 (2017) 182–191.
[42] M.R. Azhar, H.R. Abid, H. Sun, V. Periasamy, M.O. Tadé, S. Wang, One-pot synthesis of binary metal organic frameworks (HKUST-1 and UiO-66) for enhanced adsorptive removal of water contaminants, J. Colloid Interface Sci. 490 (2017) 685–694.
[43] E.D.P. Almeida, A.A. Costa, M.R. Serafini, F.C. Rossetti, J. Marchetti, V.H.V. Sarmento, R.S. Nunes, M.E.G. Valerio, A.A.S. Araú jo, A.A.M. Lira,

Preparation and characterization of chloroaluminum phthalocyanine-loaded solid lipid nanoparticles by thermal analysis and powder X-ray diffraction techniques, J. Therm. Anal. Calorim. 108 (2012) 191–196.
[44] T. Lopez, E. Ortiz, M. Alvarez, J. Navarrete, J.A. Odriozola, F.M. Ortega, E.A.P. Mozo, P. Escobar, K.A. Espinoza, I.A. Rivero, Study of the stabilization of zinc phthalocyanine in sol-gel TiO2 for photodynamic therapy applications, Nanomed. Nanotechnol. Biol. Med. 6 (2010) 777–785.
[45] X. Wang, X. Lu, L. Wu, J. Chen, 3D metal-organic framework as highly efficient biosensing platform for ultrasensitive and rapid detection of bisphenol A, Biosens. Bioelectron. 65 (2015) 295–301.
[46] K.S. Walton, R.Q. Snurr, Applicability of the BET method for determining surface areas of microporous metal-organic frameworks, J. Am. Chem. Soc. 129 (2007) 8552–8556.
[47] L.J. Wang, H. Deng, H. Furukawa, F. Gandara, K.E. Cordova, D. Peri, O.M. Yaghi, Synthesis and characterization of metal-organic framework-74 containing 2, 4, 6, 8, and 10 different metals, Inorg. Chem. 53 (2014) 5881–5883.
[48] H. Guo, Y. Zhang, Z. Zheng, H. Lin, Y. Zhang, Facile one-pot fabrication of Ag@MOF(Ag) nanocomposites for highly selective detection of 2,4,6-trinitrophenol in aqueous phase, Talanta 170 (2017) 146–151.
[49] Q. Chen, X. Li, X. Min, D. Cheng, J. Zhoua, Y. Li, Z. Xie, P. Liu, W. Cai, C. Zhang, Determination of catechol and hydroquinone with high sensitivity using MOF-graphene composites modified electrode, J. Electroanal. Chem. 789 (2017) 114–122.
[50] K.E. Ramohlola, M. Masikini, S.B. Mdluli, G.R. Monama, M.J. Hato, K.M. Molapo, E.I. Iwuoha, K.D. Modibane, Electrocatalytic hydrogen production properties of poly (3- aminobenzoic acid) doped with metal organic frameworks, Int. J. Electrochem. Sci. 12 (2017) 4392–4405.
[51] T. Fan, F. Yin, H. Wang, X. He, G. Li, A metal-organic framework/carbon composite with enhanced bifunctional electrocatalytic activities towards oxygen reduction/evolution reactions, Int. J. Hydrogen Energy 42 (2016) 17376–17385.
[52] G.K. Dedzoa, E.P. Yamboua, M.R.T. Saheua, G. Ngnieb, C.P. Nanseu-Njikia, C. Detellierb, E. Ngamenia, Hydrogen evolution reaction at PdNPs decorated 1:1 clay minerals and application to the electrocatalytic determination of P-Nitrophenol, J. Electroanal. Chem. (2017), https://doi.org/10.1016/j.jelechem.2017.07.030.
[53] B.E. Conway, Electrochemical proton transfer and cathodic hydrogen evolution, Sci. Prog. 71 (1987) 479–510.
[54] J. Yang, S. Gunasekaran, Electrochemically reduced graphene oxide sheets for use in high performance supercapacitors, Carbon N. Y. 51 (2013) 36–44.
[55] D.-N. Li, A.-J. Wang, J. Wei, Q.-L. Zhang, J.-J. Feng, Facile synthesis of flower-like Au@AuPd nanocrystals with highly electrocatalytic activity for formic acid oxidation and hydrogen evolution reactions, Int. J. Hydrogen Energy 42 (2017) 19894–19902.
[56] J. Chen, G. Xia, P. Jiang, Y. Yang, R. Li, R. Shi, J. Su, Q. Chen, Active and durable hydrogen evolution reaction catalyst derived from Pd-Doped metal-organic frameworks, ACS Appl. Mater. Interfaces. 8 (2016) 13378–13383.
[57] C. Wu, C. Li, B. Yang, S. Zhou, D. Shi, Y. Wang, G. Yang, J. He, Y. Shan, Electrospun $MnCo_2O_4$ nano fibers for efficient hydrogen evolution reaction, Mater. Res. Express. 3 (2016) 3.
[58] W. Zhou, J. Jia, J. Lu, L. Yang, D. Hou, G. Li, S. Chen, Recent developments of carbon-based electrocatalysts for hydrogen evolution reaction, Nano Energy. 28 (2016) 29–43.
[59] T. Shinagawa, A.T. Garcia-Esparza, K. Takanabe, Insight on Tafel slopes from a microkinetic analysis of aqueous electrocatalysis for energy conversion, Sci. Rep. 5 (2015), 13801.